metals

MDPI

Article

Oscillatory Precipitation and Re-Dissolution of Mn-Ni-(Si)-Based Precipitates in Aged Reactor Pressure Vessel Model Steels

Fan Yang [1], Zhiwei Cao [1], Jianbin Zhang [2] and Ting Hao [1,*]

[1] School of Mechanical Engineering, Suzhou University of Science and Technology, Suzhou 215009, China; 13801437419@163.com (F.Y.)
[2] State Key Laboratory of Advanced Processing and Recycling of Nonferrous Metals, Lanzhou University of Technology, Lanzhou 730050, China; zhangjb@lut.edu.cn
* Correspondence: hao.ting@usts.edu.cn; Tel.: +86-51268320622

Abstract

The irradiation-induced precipitation of Mn-Ni-rich precipitates (MNPs) or Mn-Ni-Si-rich precipitates (MNSPs) is the primary cause of embrittlement in reactor pressure vessel (RPV) steels. In this study, high-precision electrical resistivity (ER) measurements (10 nΩ·m accuracy) were employed to probe the thermal stability of aging-induced MNSPs in RPV model steels that were aged at 600 °C for 30 h. We report the discovery of oscillatory precipitation and re-dissolution of MNPs/MNSPs, evidenced by alternating ER peaks upon repeated thermal cycling to 950 °C. This oscillatory behavior is further confirmed by scanning transmission electron microscopy (STEM) and energy-dispersive X-ray spectroscopy (EDS) observations. Internal friction (IF) results indicate that the oscillatory precipitation and re-dissolution of MNPs/MNSPs should occur predominantly within the grain interiors rather than at grain boundaries (GBs).

Keywords: Mn-Ni-rich precipitates; grain boundaries; electrical resistivity; reactor pressure vessel steel; internal friction

1. Introduction

Nuclear power is an essential part of the global clean energy supply, supplying approximately 8% of the world's electricity generation [1]. To ensure the long-term sustainability of nuclear energy, the operational lifespan of existing light water reactors (LWRs) must be extended to 60 or even 80 years. However, neutron irradiation promotes the formation of Mn-Ni-rich precipitates (MNPs) and Mn-Ni-Si-rich precipitates (MNSPs) in reactor pressure vessel (RPV) steels, leading to significant embrittlement and hardening. Mitigating this degradation is essential for the safe and prolonged operation of in-service LWRs [2–8]. Notably, MNPs and MNSPs can be dissolved under appropriate thermal treatment conditions, which partially reverses their embrittling effects and helps extend RPV service life. For example, post-irradiation annealing (PIA) at 500 °C for 10 min was shown to reduce the volume fraction of MNSPs by about 50% and decrease their modal size from 3.2–3.4 nm to 1.8–2.2 nm in a neutron-irradiated RPV steel, as characterized by atom probe tomography (APT) [9].

However, the precipitation/dissolution mechanisms of MNPs/MNSPs at the atomic scale are still controversial and remain unclear due to the multi-component complexity of low-alloy RPV steels, the much smaller sizes, the low thermal stability of MNPs/MNSPs (~nm), and the irradiation-induced and/or aging-induced variability. Recent studies

Check for updates

Academic Editor: Arne Mattias Thuvander

Received: 19 May 2026
Revised: 11 June 2026
Accepted: 13 June 2026
Published: 14 June 2026

Copyright: © 2026 by the authors. Licensee MDPI, Basel, Switzerland. This article is an open access article distributed under the terms and conditions of the Creative Commons Attribution (CC BY) license.

revealed that the precipitation of MNPs/MNSPs can be induced or enhanced by irradiation, thermal aging or a combination of both. The resulting precipitates, including solute clusters and MNPs/MNSPs (solute clusters, Γ_2 (Mn_2Ni_3Si) and G ($Mn_6Ni_{16}Si_7$) crystalline phases, B2 MnNi ordered phases, and their mixtures), are thermodynamically stable [10–17]. Furthermore, the alloying elements (Mn, Ni, Si, Cu, etc.) in RPV steels play different roles in the precipitation and dissolution of MNPs/MNSPs. At high neutron irradiation fluence, Ni plays a dominant role in the precipitation of MNPs/MNSPs compared to Mn and Si [15], while the dissolution process is mainly driven by migration of Mn atoms from the Mn-Ni-(Si)-rich clusters. It was also found that more Ni than Mn atoms are dissolved since the Mn content in the clusters is lower than that of Ni [9].

Our previous study demonstrated that long-term aging (400–600 °C, 200 h) induces the precipitation of MNSPs, which pin grain boundary (GB) relaxation gliding and suppress the GB peak near 630 °C in the internal friction (IF) spectra, and these MNSPs dissolve upon subsequent aging at 700 °C for 200 h, resulting in the depinning of the GB peak [18]. Moreover, IF results and transmission electron microscopy (TEM) observations confirmed the precipitation of C-bearing MNSPs in the RPV model steel subjected to aging at 600 °C for 20 h [19,20]. Although studies have demonstrated that MNSPs dissolve at temperatures above 700 °C [18–20], the specific annealing conditions for dissolving MNSPs remain unclear. In this study, high-precision electrical resistivity (ER), together with the internal friction method (IF) and scanning transmission electron microscopy (STEM), are employed to monitor annealing conditions for the precipitation and re-dissolution of MNPs/MNSPs in different RPV model steels, thereby mitigating embrittlement caused by irradiation- or aging-induced MNPs/MNSPs.

2. Materials and Methods

Three types of RPV model steels as listed in Table 1 were prepared with the nominal compositions: Fe-1.35%Mn-0.74%Ni-0.19%Si (S1, all in wt.% thereafter), Fe-1.35%Mn-0.74%Ni (S2) and Fe-1.35%Mn-0.74%Ni-0.19%Si-0.1%Cu (S3). All RPV model steels were prepared in a vacuum arc melting furnace using high-purity elements and forged and rolled into thick plates. The actual composition of the typical sample S1 was determined by a direct reading spectrometer as shown in Table 2.

Table 1. Nominal compositions (wt.%) of the three RPV model steels.

Sample No.	Fe	Cu	Mn	Ni	Si
S1	Bal.	-	1.35	0.74	0.19
S2	Bal.	-	1.35	0.74	-
S3	Bal.	0.1	1.35	0.74	0.19

Table 2. Actual composition (wt.%) of the as-prepared Fe-1.6%Mn-1.0%Ni-0.2%Si (S1) RPV model steel.

Elements	Mn	Ni	Si	C	S	P	Cu	Fe
Content	1.614	1.018	0.206	<0.004	0.004	0.003	0.009	Bal.

The above as-prepared samples (S1, S2, S3) were aged at 600 °C for 30 h (A600), aiming for a higher nucleation density of MNPs/MNSPs. All the aged samples were furnace-cooled to room temperature (RT). The samples (S1, S2, S3) subjected to the aging are denoted as S1-A600, S2-A600, and S3-A600, respectively.

A high-precision four-probe resistivity tester (RMS-1000P, BALAB, Wuhan, China) was employed to measure ER in the temperature range between 20 °C and 900 °C with heating rates of 2–5 °C/min in a vacuum of 10 Pa maintained by the mechanical pump. Between successive heating cycles, the samples were furnace-cooled back to room temperature

under the same vacuum condition. The experiment utilized a four-point probe spaced 2.8 mm apart, and an input current of 100 mA was used during the tests. The measurement accuracy of electrical resistivity values can reach 10 nΩ·m. The size of all samples was $14 \times 4 \times 1$ mm^3, and ER (ρ (Ω·m)) is calculated by the following relationship.

$$\rho = \frac{wt}{d} \cdot R \quad (1)$$

where R (Ω) is the actual electrical resistance of the measured sample, w (mm) and t (mm) are the width and thickness of the sample, respectively, and d (mm) is the distance between two probes.

IF measurements were conducted using a multi-functional inverted pendulum instrument (MFP-1000, developed by the Institute of Solid State Physics, Chinese Academy of Sciences, Hefei, China) in a vacuum of 10 Pa with a maximum strain amplitude of 2×10^{-5} at different frequencies (0.5, 1.0, 2.0, 4.0 Hz) in the temperature range between 20 °C and 700 °C with a heating rate of 3 °C/min. The size of all IF samples was $45 \times 2 \times 1$ mm^3.

Vickers hardness measurements were carried out at RT using a 7MHVS-1000A indentation tester (Trojan, Suzhou, China). An applied load of 200 g was maintained for a holding time of 15 s. Each sample was tested with a minimum of 10 indents to obtain an average value and ensure measurement precision. Error bars represent the standard deviation.

Phase identification was performed using a Bruker D8 Advance (Bruker, Karlsruhe, Germany) X-ray diffractometer (XRD) with Cu Kα radiation operated at 40 kV and 40 mA. The diffraction patterns were collected in θ–2θ scanning mode over a 2θ range of 5–90°. The scan was performed at a rate of 0.026°/s. For microstructural characterization, a FEI Tecnai F20 STEM (FEI, Eindhoven, The Netherlands) operated at 200 keV and equipped with an energy-dispersive X-ray spectroscopy (EDS) detector was used for elemental mapping and point analysis. High-angle annular dark field (HAADF) imaging and EDS elemental mapping and point analysis were performed to reveal the spatial distribution and composition of precipitate phases.

3. Results

Figure 1a shows the ER curves of the as-received (AR) Fe-1.6%Mn-1.0%Ni-0.2%Si (S1) steel under different heating rates. A distinct peak appears in the 750–850 °C range only at the heating rate of 2 °C/min, whereas no peak is observed at 3 or 5 °C/min. The pronounced dependence on the heating rate indicates that the process responsible for the peak in the ER curve is kinetic in nature, and that higher heating rates at 3 and 5 °C/min do not provide conditions sufficient for detectable microstructural changes or phase transformations in the AR sample.

According to the isothermal transformation diagram (TTT diagram) originated from IF experimental results, the shortest time is about 30 h at the "nose" temperature of the TTT curve (600 °C) under the transformation fraction of the precipitated MNSPs phase f = 70% in a RPV model steel [20]; therefore, the present as-prepared samples (S1, S2, S3) were aged at 600 °C for 30 h (A600), aiming for a higher nucleation density of MNPs/MNSPs. Figure 1b–d show the ER curves of S1-A600, S2-A600, S3-A600 samples at a heating rate of 3 °C/min, respectively. For the case of S1-A600, as shown in Figure 1b, a weak peak appears on the curve of the S1-A600 sample in the 800–870 °C range, which is similar to the case of that in the S1-AR sample at 2 °C/min in Figure 1a. This indicates that the aging at 600 °C for 30 h was an incubation period of Mn-Ni-Si-rich clusters or precipitates, which does not give rise to a visible increase in ER value, while subsequent heating at 3 °C/min in Figure 1b further promotes the precipitation and dissolution of MNSPs in the range of 800–870 °C. Figure 1b also shows an interesting finding: the ER peak appeared (first and third heating) and disappeared (second and fourth heating) when the S1-A600 sample was

repeatedly heated to 950 °C, implying an oscillatory behavior involving the precipitation and dissolution of MNSPs. It is worth noting that there are two peaks at 840 °C and 855 °C in both the first and third heating curves, although the second peak at 855 °C in the first heating curve is extremely weak.

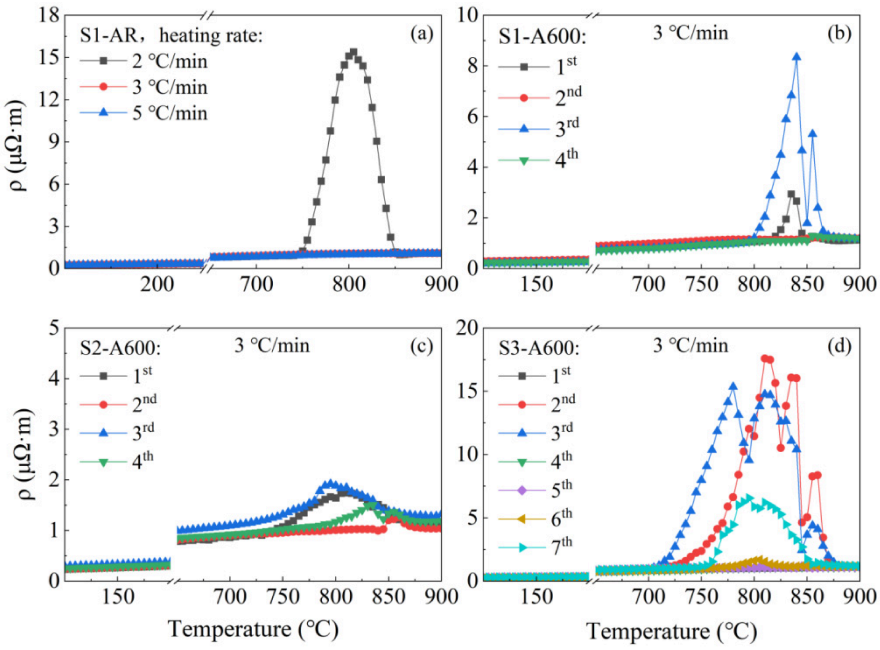

Figure 1. ER curves for RPV model steels: (**a**) S1-AR at heating rates of 2, 3, and 5 °C/min; (**b**) S1-A600, (**c**) S2-A600, and (**d**) S3-A600 during repeated heating cycles to 950 °C at 3 °C/min.

To verify the universality of this phenomenon, Figure 1c shows the ER curves of the S2-A600 sample. Analogous to the S1-A600 sample, a distinct peak emerges within the 730–860 °C range during the first and third heating cycles, whereas only a much weaker peak is observed during the second and fourth cycles. The peak is located at 795 °C during the first cycle, roughly 40 °C lower than the first peak temperature of S1-A600. Furthermore, unlike the dual-peak structure observed in S1-A600, the S2-A600 sample exhibits only a single broad peak. The ER peak intensity of S2-A600 is approximately 1.92 μΩ·m, significantly lower than the 8.3 μΩ·m of S1-A600. Although direct comparison of peak heights is complicated by differences in peak width and temperature, the pronounced contrast clearly indicates a weaker precipitation/dissolution process in the Si-free S2-A600 sample. This implies fundamental differences in the precipitate types formed in the two samples, S1-A600 and S2-A600, as will be detailed in Section 4.

For the case of the S3-A600 sample containing Cu, the precipitation/re-dissolution process becomes more complicated as there are almost no or weak peaks in the first, fourth, fifth, and sixth curves, but three strong peaks in the second curve (i.e., reaches approximately 17.6 μΩ·m for the first peak), four peaks in the third curve and a broad peak in the seventh curve in the range of 710–880 °C, as shown in Figure 1d, suggesting that an oscillatory precipitation/re-dissolution of MNSPs occurs in the S3-A600 sample, similar to the behavior observed in the S1-A600 and S2-A600 samples. All ER measurements were repeated three times; the peak temperature varied within ±5 °C and the peak amplitude within ±0.6 μΩ·m.

Abundant experimental results confirmed that the precipitation of nanoparticles plays a key role in age hardening kinetics and ultimately enhances the hardening response in many Fe-based alloys including low-alloying steels such as aged Fe-1.6%Mn-1.0%Ni-0.2%Si, Fe-1.5%Ni-0.5%Al-1.5%Mn, Fe-2.5%Cu-1.5%Ni-0.5%Al-1.5%Mn, and so on [18,21,22]. To investigate the effect of the above oscillatory precipitation/re-dissolution of MNSPs observed

in ER curves on hardening response, Vickers microhardness measurements were performed on S1-AR, S1-A600, and S1-A600 after the first to third heating cycles. As shown in Figure 2, the microhardness of the S1-A600 sample is about 115 HV, which is slightly higher than 112 HV of the S1-AR sample, indicating a weak precipitation hardening due to the aging-induced MNSPs. The microhardness of S1-A600 following the first ER heating cycle decreases from 115 HV to 110 HV, which can be attributed to the dissolution of precipitated MNSPs during heating up to 950 °C. However, the microhardness of S1-A600 increased gradually to 112 HV and 115 HV after the second and third ER heating cycles, respectively, indicating that no evident oscillatory behavior was observed in the hardness response.

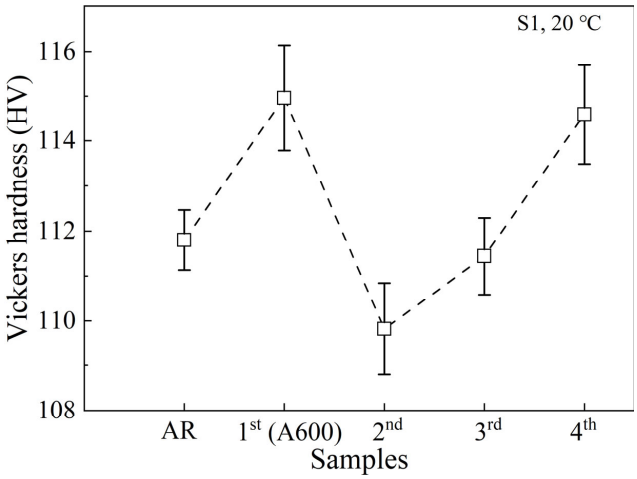

Figure 2. Vickers microhardness of S1 samples in the AR condition and before the first–fourth heating cycles.

Figure 3 displays the XRD patterns of the S1 samples. All observed diffraction peaks correspond to the α-Fe phase (PDF No. 98-000-0259); specifically, in the (110), (200), and (211) reflections, no diffraction peaks from γ-Fe are detected. Neither aging at 600 °C nor repeated heating cycles to 950 °C induce detectable secondary phases, suggesting that the precipitation of MNSPs lies below the detection limit of conventional XRD. This finding aligns with the precipitates' nanoscale dimensions (~1–3 nm) and low volume fraction [23].

To confirm the above oscillatory precipitation and dissolution phenomenon, STEM observations were performed for S1-A600 (aged-only) and S1-A600-1st (after the first ER heating cycle) samples. Figure 4 shows their high-angle annular dark field images (HAADF, a and c) and corresponding EDS mapping results (b and d) for S1-A600 and S1-A600-1st. In the S1-A600 sample (Figure 4a,b), a visible Mn-Si-rich region is observed within the grain interior. Bright-field and dark-field TEM images of the Mn-Si-rich precipitates as well as SAED patterns in Figure 5a,b verify that these precipitates possess a complete crystalline structure. It is noteworthy that no Ni enrichment is detected in Mn-Si-rich precipitates. Similar Mn-Si-rich regions were observed in other areas. In contrast to S1-A600, no evident elemental segregations or Mn-Si-rich precipitates were observed in the S1-A600-1st sample, as shown in the HAADF image in Figure 4c and the EDS mapping with a uniform distribution of Mn, Ni, and Si elements across the entire scanning area in Figure 4d, although a large number of regions were examined. Figure 6a,c,e show the bright-field images of several typical regions and their additional EDS point measurements at the corresponding locations (Figure 6b,d,f). The absence of detectable Mn-Si-rich precipitates in the S1-A600-1st sample indicates the complete dissolution of the precipitates originally present in the solely aged S1-A600 sample after a single heating cycle to 950 °C. The direct microstructural observation in Figure 6 confirms the re-dissolution of Mn-Si-rich precipitates during the oscillatory process identified in the ER results, as shown in Figure 1b.

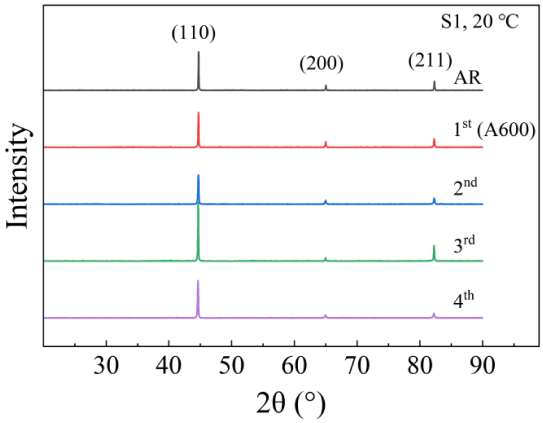

Figure 3. XRD patterns of S1 samples in the AR condition and before the first–fourth heating cycles.

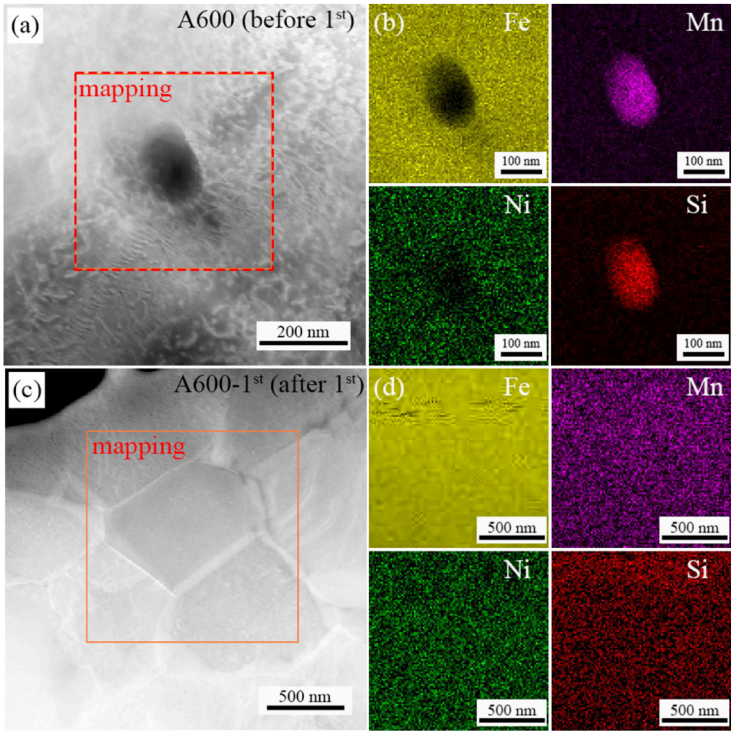

Figure 4. (**a**,**c**) High-angle annular dark-field (HAADF) images corresponding to S1-A600 before and after the first heating cycle. (**b**,**d**) EDS mapping results of Fe, Mn, Ni, and Si, from the boxed regions.

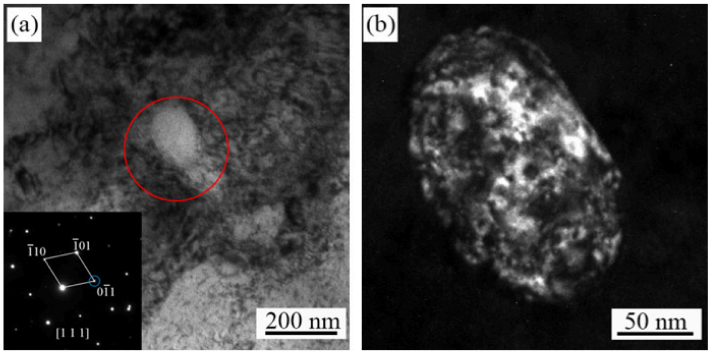

Figure 5. (**a**) Bright-field and (**b**) dark-field TEM images of the aged S1-A600 sample. The selected area electron diffraction (SAED) pattern corresponded to the red circle, and the dark-field image was taken using the reflection marked with the blue circle.

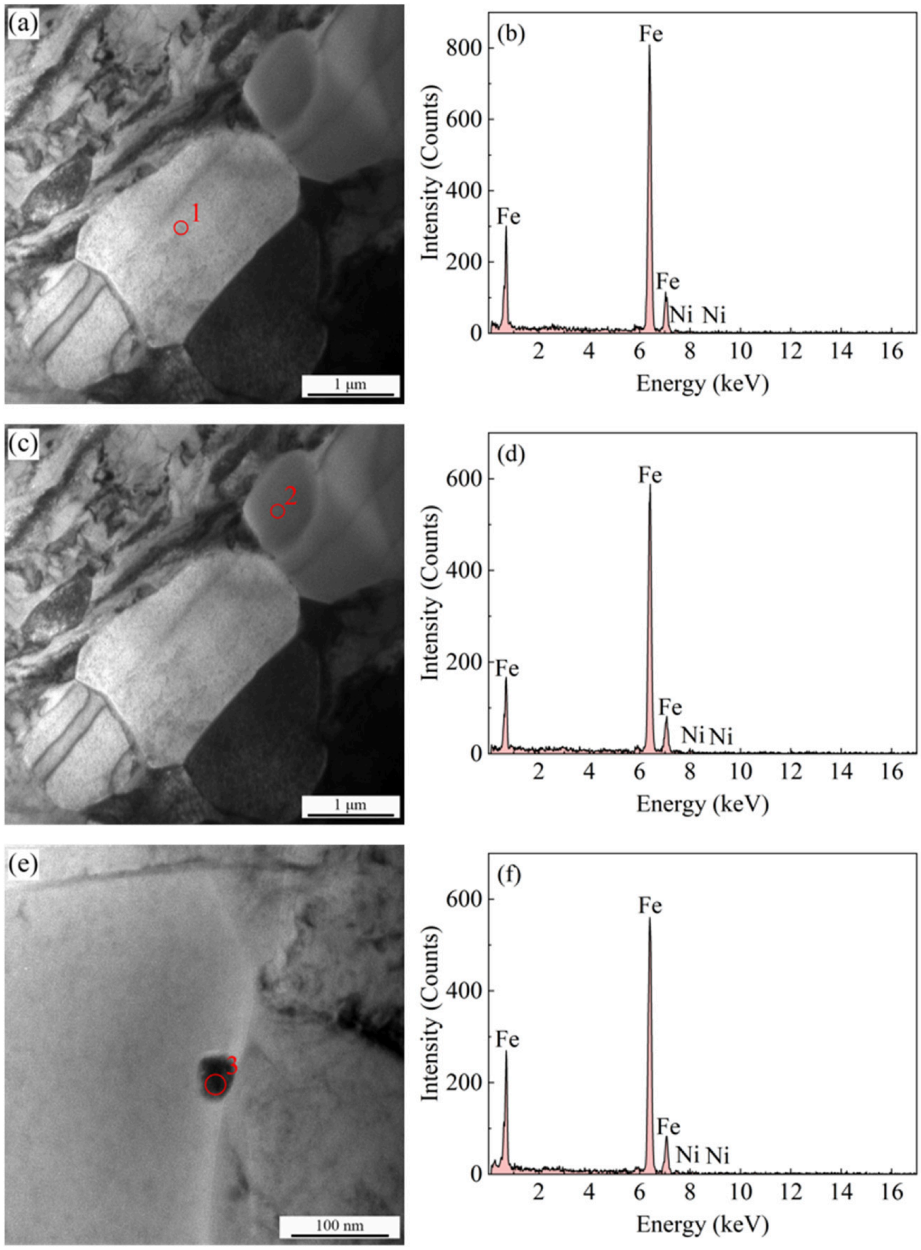

Figure 6. (**a**,**c**,**e**) Bright-field images of the S1-A600-1st sample showing the acquisition areas for EDS analysis. (**b**,**d**,**f**) EDS spectra corresponding to points 1–3.

To further understand the formation mechanism of MNPs/MNSPs, IF measurements were performed on S1-AR and S1-A600 samples. Figure 7a shows the IF spectra of the S1-AR sample measured at frequencies of 0.5, 1, 2, and 4 Hz. An obvious IF peak is observed in the 400–600 °C range in the heating curves, and the peak positions shift toward higher temperatures with increasing frequency, indicating a typical relaxation feature. This peak is identified as a GB relaxation peak associated with GB sliding [18]. Figure 7b shows the IF spectra at 1 Hz for the S1-AR and S1-A600 samples during four heating cycles to 950 °C (corresponding to those in Figure 1b). Compared with the Q^{-1} value ($Q^{-1} \approx 6.7 \times 10^{-2}$ at 532 °C) for the S1-AR sample, all Q^{-1} values ($Q^{-1} \approx 3.9 \times 10^{-2}$ at 532 °C) for the S1-A600 sample after the first–fourth heating cycles exhibit distinct decreases, suggesting a pronounced pinning effect on GB sliding due to the preferential precipitation of MNSPs along GBs induced by the present aging treatment.

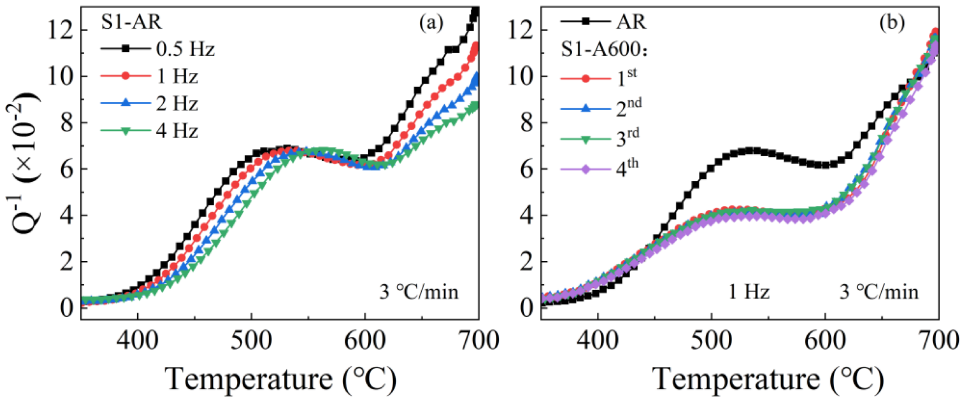

Figure 7. (**a**) Temperature-dependent IF (Q^{-1}) curves at four different frequencies of 0.5, 1, 2, and 4 Hz for continuous heating with a rate of 3 °C/min for the S1-AR sample. (**b**) Temperature-dependent IF (Q^{-1}) curves at 1 Hz with a heating rate of 3 °C/min for the S1-AR, S1-A600-1st to 4th samples.

4. Discussion

According to Matthiessen's rule, the ER of metal materials can be represented by the following relationship [24,25]:

$$\rho_T = \rho_T^{alloy} + \Delta\rho_T^{Vac.}\cdot N_V + \Delta\rho_T^{disl.}\cdot L_V + \Delta\rho_T^{GB}\cdot S_V \quad (2)$$

$$\rho_T^{alloy} = \rho_T^{pure} + \sum_i^n \Delta\rho_T^i\cdot C^i \quad (3)$$

where, ρ_T (Ω·m) is electrical resistivity of the used alloy measured at T (°C). $\Delta\rho_T^{Vac}$ (Ω·m/at. fraction), $\Delta\rho_T^{disl.}$ (Ω·m^3), and $\Delta\rho_T^{GB}$ (Ω·m^2) represent the unit concentration/density of vacancy, dislocation, and GBs to ρ, respectively. N_V, L_V, and S_V correspond to vacancy concentration, dislocation density, and GB density. ρ_T^{pure} is the ρ_T value of a single crystalline pure metal without defects. $\Delta\rho_T^i$ and C^i denote the contribution per unit concentration of the i-th alloying element to ρ_T and its concentration, respectively.

As shown in Figure 1a, the ER response of the S1-AR sample during heating at 2 °C/min exhibits a peak defined by two stages: the sharp ascending stage of this peak starting at about 750 °C in the ER curve at a heating rate of 2 °C/min can be mainly attributed to the formation of abundant new Mn-Ni-Si-rich clusters or phase interfaces $(\Delta\rho_T^{GB}\cdot S_V)$, while a sudden descending stage of this peak ending at about 850 °C should correspond to the annihilation of new Mn-Ni-Si-rich clusters or phase interfaces at higher temperatures. It should be noted that the ER peak likely corresponds to the α-Fe to γ-Fe phase transformation according to Ref. [26]. This transformation typically occurs at a relatively fixed temperature, followed by a monotonic increase in ER. However, the ER peak observed in our study shows a markedly different trend.

The ER peak appears only at a heating rate of 2 °C/min in the AR sample, demonstrating that thermal vacancies during heating facilitate Mn-Ni-Si-rich precipitation and that sufficient time for their generation is essential. The slight increase in the baseline of the ER curve with temperature can be attributed to the sum of the other terms (ρ_T^{alloy}, $\Delta\rho_T^{Vac.}$, N_V, $\Delta\rho_T^{disl.}\cdot L_V$), all of which vary smoothly with temperature. It should be noted that these alternative factors are not directly responsible for the ER peak itself, although thermal vacancies are known to promote Mn-Ni-Si-rich precipitation. Notably, according to Ref. [27], vacancy concentration variations induced by 0.154 dpa neutron irradiation in a commercial RPV steel resulted in a resistivity increase of only ~0.4 μΩ·m, which is far lower than the ~8.3 μΩ·m of the ER peak observed here. Therefore, we infer that the effect of vacancy concentration on the ER peak is negligible compared to that of precipitate/matrix interfaces. Thus, the ER peak likely reflects the dynamic process of

fine-scale MNSPs precipitation and dissolution, which is associated with a substantial increase and subsequent decrease in grain boundary density. This aligns with earlier internal friction (IF) analyses [18,20].

Unlike the S1-AR sample, which exhibited no discernible ER peak during heating at 3 °C/min, the S1-A600 sample displayed a weak peak in the 800–870 °C range during its first heating scan at 3 °C/min. This observation implies that the preceding aging treatment at 600 °C for 30 h served as an incubation period, which did not raise the ER value but rendered the microstructure susceptible to subsequent precipitation and dissolution upon reheating. The alternating appearance (first and third heating) and disappearance (second and fourth heating) of the ER peak upon repeated ER heating cycles confirms the oscillatory precipitation and re-dissolution of MNSPs in S1-A600. That is, the peak appears in the first and third heating cycles when precipitation and re-dissolution take place; its absence in second and fourth heating cycles means that these processes are suppressed, likely because the prior heating to 950 °C in first and third heating cycles eliminates the necessary nucleation sites or reduces solute supersaturation. This alternating pattern cannot be attributed to thermal hysteresis or reversible ordering/disordering, as such mechanisms would produce a similar peak in every cycle under identical conditions. Instead, it can be rationalized as follows: As shown in Figure 4, the subsequent dissolution of MNSPs after the first heating cycle leads to a more homogeneous solute distribution. During the second heating, this uniform solute field delays precipitation beyond the time window set by the heating rate, preventing the appearance of an ER peak. The subsequent cooling after the second heating likely allows for solute atoms to form new fine clusters, which serve as nuclei for re-precipitation in the third cycle. In the third heating cycle, the ER peak consists of two sub-peaks resolved at 840 °C and 855 °C; although a definitive phase identification would require additional diffraction analysis, these peaks can be tentatively correlated with the precipitation and dissolution of Γ_2 (Mn_2Ni_3Si) and G ($Mn_6Ni_{16}Si_7$) crystalline phases according to the references [11,16]. We surmise that the phase interfaces (primarily manifesting as $\Delta\rho_T^{GB}\cdot S_V$) generated during the precipitation and dissolution of Γ_2 (Mn_2Ni_3Si) and G ($Mn_6Ni_{16}Si_7$) crystalline phases play a dominant role in the appearance and disappearance of the ER peak, although higher-resolution techniques are required for definitive phase identification.

Figure 8 plots the room-temperature (RT, 20 °C) ER values for S1-AR and the S1-A600 samples subjected to first to fourth heating cycles. According to Matthiessen's rule in Equation (3), the alloying-term ($\sum_i^n \Delta\rho_T^i\cdot C^i$) for the S1-AR sample (actual composition in Table 2) is calculated to be 0.218 μΩ·m, based on the specific resistivities of Mn, Ni, and Si in dilute Fe-based alloys, as shown in Table 3 [28–30]. The measured ER values at RT in Figure 8 align closely with the calculated alloying term ($\sum_i^n \Delta\rho_T^i\cdot C^i$) ER value, indicating that this term constitutes the majority of the total ER baseline observed in Figure 1. In contrast, the anomalously high ER values at the peaks within the 800–870 °C range during the first and third heating cycles (i.e., 8.3 μΩ·m at 840 °C in Figure 1b) are attributed to electron scattering at the additional grain boundary interfaces generated by the precipitation/dissolution of MNSPs. As shown in Figure 8, a key observation is that the room-temperature (RT) ER value of the A600-3rd sample shows a decrease to 0.18 μΩ·m, which is 0.04 μΩ·m lower than for the initial S1-AR sample (0.22 μΩ·m). Subsequently, the value partially recovers to about 0.21 μΩ·m in the A600-4th cycle, exhibiting oscillatory behavior with repeated thermal cycling. However, this RT ER oscillation does not completely synchronize with the ER peak behavior, suggesting that the oscillatory ER peaks reflect a distinct and dynamic microstructural evolution. This discrepancy, along with the asynchronous behavior observed in both RT ER (Figure 8) and Vickers hardness (Figure 2), suggests that the precipitation/dissolution process induces significant mod-

ifications in other contributing terms ($\Delta\rho_T^{Vac.}$, N_V, $\Delta\rho_T^{disl.}\cdot L_V$) beyond the alloying term ($\rho_T^{pure} + \sum_i^n \Delta\rho_T^i \cdot C^i$) during the precipitation/dissolution process of MNSPs.

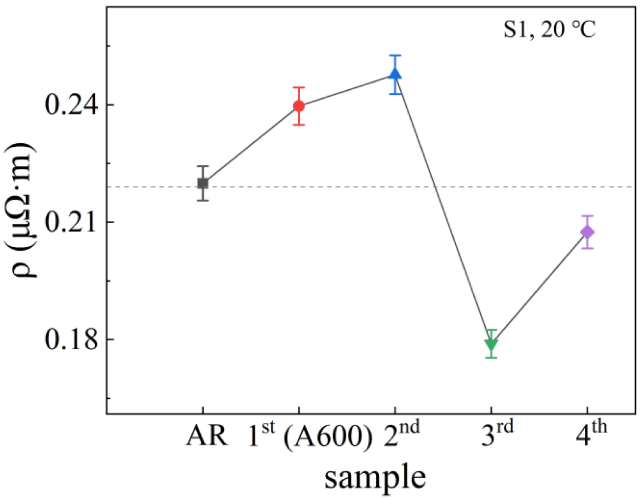

Figure 8. ER at 20 °C for S1-AR and S1-A600 before the first–fourth heating cycles. All data points exhibit a standard deviation < 0.01 μΩ·m, with error bars magnified for visibility. The dashed line represents the calculated theoretical ER value of S1-AR sample at 20 °C according to the Matthiessen's rule.

Table 3. Atomic concentrations and $\Delta\rho_T^i$ used for Matthiessen's rule.

Element	Concentration (wt.%)	$\Delta\rho_T^i$ (μΩ·m/wt.%) for Binary Alloys	References
Mn	1.614	0.046	[28,30]
Ni	1.018	0.024	[28,30]
Si	0.206	0.117	[29,30]

STEM-EDS analysis confirms the formation of Mn-Si-rich precipitates following aging and their subsequent dissolution after a single heating cycle as shown in Figure 4. This microstructural evolution aligns with the elevated ER of 0.24 μΩ·m observed in S1-A600 compared to the 0.22 μΩ·m of S1-AR at 20 °C in Figure 8. However, the absence of detectable Ni enrichment in Figure 4b appears inconsistent with the proposed formation of Ni-bearing Γ_2 (Mn_2Ni_3Si) and G ($Mn_6Ni_{16}Si_7$) phases. This apparent contradiction can be rationalized by considering two key factors: (i) the intrinsically low diffusivity of Ni in α-Fe likely retards its incorporation relative to Mn and Si, resulting in initially Mn-Si-rich precipitates; (ii) finer-scale, Ni-enriched MNSPs may exist but remain obscured by the dominant Mn-Si signal in EDS mapping [19]. Thus, the potential co-existence of Ni-containing phases cannot entirely be ruled out in the precipitation period of MNP formation. The disappearance of the ER peak in the second cycle (Figure 1b), associated with the re-dissolution of MNPs, provides direct microstructural validation of the oscillatory precipitation and dissolution behavior. To visualize these key microstructural changes, combining the current STEM observation and the internal friction (IF) measurements in Figure 7, a schematic diagram is presented in Figure 9.

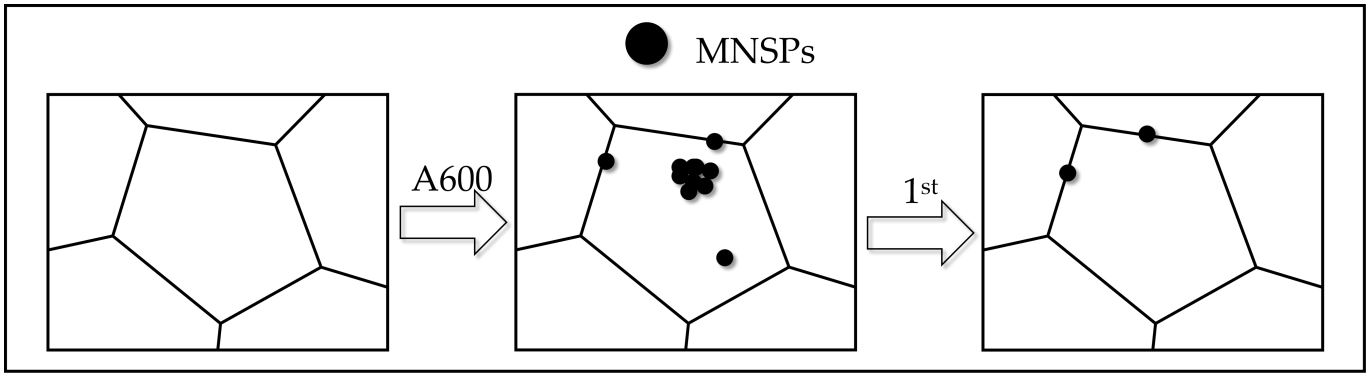

Figure 9. Schematic illustration of the microstructural evolution mechanisms revealed by STEM observations and internal friction (IF) measurements.

The single broad ER peak in the first and third cycles in Figure 1c indicates that the absence of Si fundamentally alters the precipitation pathway, resulting in the precipitation and re-dissolution of MNPs (MnNi or Mn_2Ni phases) [31]. The width and asymmetry of the peak reflect the kinetic distribution associated with MnNi and/or Mn_2Ni precipitation/dissolution, indicating that the single broad ER peak likely comprises multiple distinct phases. The reduced peak temperature (795 °C during the first cycle in Figure 1c), which is approximately 40 °C lower than that of S1-A600 (Figure 1b), implies that these MNPs possess lower thermal stability than the MNSPs. This demonstrates that Si plays an important role in stabilizing the more complex Mn-Ni-Si-rich phases, consequently leading to a higher peak temperature and a larger peak amplitude in the S1 sample (Figure 1b). It is also noticeable that the ER peaks in the S2-A600 sample (without Si) oscillate across repeated heating cycles from the first to fourth cycle. This behavior implies differing diffusivities of Ni and Mn in Fe during the formation of MNPs (MnNi or Mn_2Ni phases). A detailed phase analysis will be addressed in future work.

The multiple strong ER peaks observed in Figure 1d indicate that the addition of Cu significantly enhances MNSPs precipitation and leads to a more complex precipitation and re-dissolution process. Owing to its low solubility in α-Fe, Cu readily forms Cu-rich precipitates (CRPs) during the early stages of irradiation and thermal aging. According to APT studies [15] and kinetic Lattice Monte Carlo simulations [32], CRPs (with a Cu-rich core) act as heterogeneous nucleation sites, promoting the development of a complex composite structure with the surrounding Mn-Ni-Si-rich shell. This coupled entity ultimately evolves into more stable phases, such as the G phase or the Γ_2 phase [15,32–34]. Furthermore, the complexity of the precipitation and re-dissolution phenomenon in the Cu-containing S3-A600 sample can be attributed to Cu-enhanced MNSP nucleation, as Cu reduces interface formation energy and interacts energetically with Ni/Mn [32–36].

In a word, the above ER results in Figure 1 lead to three principal conclusions: First, thermal aging at 600 °C for 30 h serves as a critical incubation period for the nucleation of MNPs or MNSPs in the aforementioned RPV model steels. Second, subsequent heating to 950 °C during ER measurement significantly promotes their precipitation and dissolution. Third, the absence of Si suppresses MNP formation in the S2-A600 sample, whereas the presence of Cu catalyzes the initial precipitation of MNSPs in S3-A600, corroborating previous findings on Cu-containing RPV steels [15].

IF results provide further insight into the spatial origin of this oscillatory behavior. The pronounced decrease in Q^{-1} from 6.7×10^{-2} (S1-AR) to 3.9×10^{-2} (S1-A600) indicates that the aging at 600 °C for 30 h induces a strong pinning effect on GB sliding due to the preferential precipitation of MNSPs along GBs induced by the present aging treatment [18]. Notably, the oscillatory precipitation and re-dissolution of MNSPs are clearly reflected in

the ER peaks during the repeated heating cycles in Figure 1b, whereas the GB relaxation peak remains essentially unchanged ($Q^{-1} \approx 3.9 \times 10^{-2}$ at 532 °C at 1 Hz) throughout all cycles (Figure 7b). This is further supported by the STEM observations, in which no visible MNPs/MNSPs are detected at GBs (Figures 4c,d and 6). The contrast between the stable GB pinning effect and the pronounced ER peaks, coupled with the absence of visible GB precipitates in STEM observations, indicates that the oscillatory precipitation and dissolution are confined to the grain interiors. Meanwhile, the fine-scale Mn-Ni-Si-rich clusters at GBs, which are too tiny to observe via STEM, appear to remain thermally stable throughout the repeated thermal cycles. The apparent contradiction lies in the stability of Mn-Ni-Si-rich clusters at GBs (evidenced by unchanged Q^{-1} values) despite the oscillatory precipitation and dissolution occurring in the grain interior (shown by alternating ER peaks from the first to fourth cycle). The underlying cause is likely the kinetic difference in cluster behavior between the two regions. Previous studies provide relevant evidence: the GB relaxation peak disappears entirely in the Fe-1.6%Mn-1.0%Ni-0.2%Si (wt.%) alloy aged at 600 °C for 200 h [18], and Mn-Si-rich precipitates are still partly present in the Fe-1.0%Mn-0.4%Ni-0.2%Si (wt.%) alloy after the annealing at 800 °C for 1 h [37]. These findings suggest that Mn-Ni-Si-rich clusters exhibit significantly slower precipitation/dissolution kinetics at GBs compared to within the grain interior.

The oscillatory precipitation and re-dissolution within grain interiors offers a refined perspective for PIA strategies. The present results directly demonstrate that MNSPs dissolve during heating to 950 °C, yet re-precipitate within grain interiors upon subsequent reheating. This finding is consistent with APT observations showing that the annealing of RPV steels typically results in only partial dissolution of precipitates, accompanied by coarsening of the undissolved fraction [38]. Practically, this suggests that optimizing annealing conditions is crucial for effective mechanical property recovery. Specifically, utilizing the identified dissolution temperature window (800–870 °C), in conjunction with controlled heating and cooling rates, could facilitate sufficient dissolution of MNPs/MNSPs.

5. Conclusions

In this study, the precipitation and re-dissolution of MNPs/MNSPs were systematically investigated in three aged RPV model steels (600 °C, 30 h) via ER, STEM, and IF techniques. High-precision ER measurements revealed oscillatory precipitation/dissolution behavior of MNPs/MNSPs, highly sensitive to Si and Cu content, which was directly validated by STEM-EDS observations for the aged S1-A600 sample. The GB relaxation peak observed in IF measurements (450–600 °C) suggests that the aging treatment (600 °C, 30 h) resulted in the formation of fine-scale MNPs/MNSPs in GBs, which partially pin GB sliding. In contrast, the oscillatory precipitation and dissolution behaviors observed during ER heating cycles up to 950 °C appear to be confined to the grain interiors rather than at GBs. These findings enhance the fundamental understanding of aging- and irradiation-induced precipitation, clarify the underlying mechanisms, and provide critical insights for optimizing post-irradiation annealing strategies to mitigate embrittlement and extend RPV service life.

Author Contributions: Conceptualization, T.H. and F.Y.; methodology, F.Y.; validation, F.Y., T.H. and Z.C.; formal analysis, F.Y., T.H. and J.Z.; investigation, F.Y.; resources, J.Z. and T.H.; data curation, F.Y.; writing—original draft preparation, F.Y.; writing—review and editing, F.Y. and T.H.; visualization, F.Y. and Z.C.; supervision, T.H.; project administration, T.H.; funding acquisition, T.H. All authors have read and agreed to the published version of the manuscript.

Funding: This research was funded by the National Natural Science Foundation of China, grant number 12575297, 12075274, 11775255.

Data Availability Statement: The original contributions presented in this study are included in the article. Further inquiries can be directed to the corresponding author.

Conflicts of Interest: The authors declare no conflicts of interest.

Abbreviations

The following abbreviations are used in this manuscript:

MNSPs	Mn-Ni-Si-rich precipitates
MNPs	Mn-Ni-rich precipitates
RPV	reactor pressure vessel
ER	electrical resistivity
STEM	scanning transmission electron microscopy
EDS	energy dispersive X-ray spectroscopy
IF	internal friction
GB	grain boundary
PIA	post-irradiation annealing
APT	atom probe tomography
HAADF	High-angle annular dark field
AR	as-received

References

1. International Energy Agency. Global Energy Review 2025. Available online: https://www.iea.org/reports/global-energy-review-2025 (accessed on 13 October 2025).
2. Odette, G.R.; Yamamoto, T.; Williams, T.J.; Nanstad, R.K.; English, C.A. On the history and status of reactor pressure vessel steel ductile to brittle transition temperature shift prediction models. *J. Nucl. Mater.* **2019**, *526*, 151863. [CrossRef]
3. Jacobs, R.; Yamamoto, T.; Odette, G.R.; Morgan, D. Predictions and uncertainty estimates of reactor pressure vessel steel embrittlement using Machine learning. *Mater. Des.* **2023**, *236*, 112491. [CrossRef]
4. Glade, S.C.; Wirth, B.D.; Odette, G.R.; Asoka-Kumar, P. Positron annihilation spectroscopy and small angle neutron scattering characterization of nanostructural features in high-nickel model reactor pressure vessel steels. *J. Nucl. Mater.* **2006**, *351*, 197–208. [CrossRef]
5. Kamboj, A.; Almirall, N.; Yamamoto, T.; Tumey, S.; Marquis, E.A.; Odette, G.R. Dose and dose rate dependence of precipitation in a series of surveillance RPV steels under ion and neutron irradiation. *J. Nucl. Mater.* **2024**, *588*, 154772. [CrossRef]
6. Wang, W.; Li, B.; Fu, M.; Jia, W.; Quan, Q.; Liu, X.; Liu, W. The evolution of NiMnSi clusters in RPV steels under proton irradiation: The effect of Cu. *J. Nucl. Mater.* **2026**, *618*, 156174. [CrossRef]
7. Guo, Z.; Liu, X.; Wu, S.; Gao, S.; Liu, W. Calculation of the critical nucleus size and minimum energy path of T3 phase in Fe-Mn-Ni-Si alloys: An integrated phase-field and constrained string method. *Comput. Mater. Sci.* **2025**, *258*, 114095. [CrossRef]
8. Li, B.; Zhou, M.; Zhang, Y.; Zhang, X. Effect of pulse current on the evolution of Cu-Mn-Ni precipitate in copper-rich RPV model steel under cyclic irradiation. *J. Nucl. Mater.* **2025**, *616*, 156015. [CrossRef]
9. Styman, P.D.; Hyde, J.M.; Parfitt, D.; Wilford, K.; Burke, M.G.; English, C.A.; Efsing, P. Post-irradiation annealing of Ni-Mn-Si-enriched clusters in a neutron-irradiated RPV steel weld using Atom Probe Tomography. *J. Nucl. Mater.* **2015**, *459*, 127–134. [CrossRef]
10. Nagai, Y.; Toyama, T.; Nishiyama, Y.; Suzuki, M.; Tang, Z.; Hasegawa, M. Kinetics of irradiation-induced Cu precipitation in nuclear reactor pressure vessel steels. *Appl. Phys. Lett.* **2005**, *87*, 261920. [CrossRef]
11. Whiting, T.M.; King, D.J.M.; Wenman, M.R. On the formation and structure of Mn-Ni-Si Γ_2 precipitates in steels. *J. Nucl. Mater.* **2020**, *542*, 152429. [CrossRef]
12. Almirall, N.; Wells, P.B.; Ke, H.; Edmondson, P.; Morgan, D.; Yamamoto, T.; Odette, G.R. On the Elevated Temperature Thermal Stability of Nanoscale Mn-Ni-Si Precipitates Formed at Lower Temperature in Highly Irradiated Reactor Pressure Vessel Steels. *Sci. Rep.* **2019**, *9*, 9587. [CrossRef] [PubMed]
13. Styman, P.D.; Hyde, J.M.; Wilford, K.; Morley, A.; Smith, G.D.W. Precipitation in long term thermally aged high copper, high nickel model RPV steel welds. *Prog. Nucl. Energy* **2012**, *57*, 86–92. [CrossRef]
14. Ke, H.; Wells, P.; Edmondson, P.D.; Almirall, N.; Barnard, L.; Odette, G.R.; Morgan, D. Thermodynamic and kinetic modeling of Mn-Ni-Si precipitates in low-Cu reactor pressure vessel steels. *Acta Mater.* **2017**, *138*, 10–26. [CrossRef]
15. Wells, P.B.; Yamamoto, T.; Miller, B.; Milot, T.; Cole, J.; Wu, Y.; Odette, G.R. Evolution of manganese-nickel-silicon-dominated phases in highly irradiated reactor pressure vessel steels. *Acta Mater.* **2014**, *80*, 205–219. [CrossRef]

16. Liu, H.; Li, Q. The characterization of a nanoscale MnNi cluster in thermally aged reactor pressure vessel steels. *Mater. Res. Express* **2022**, *9*, 026531. [CrossRef]
17. Liu, X.; Guo, Z.; Wu, S.; Liu, W. Effects of Si on the precipitate of MNSPs in Fe-Mn-Ni-Si Quinary System: A phase-field simulation. *Nucl. Instrum. Methods Phys. Res. Sect. B Beam Interact. Mater. At.* **2025**, *566*, 165755. [CrossRef]
18. Wu, Y.; Hao, T.; Sun, M.; Jiang, W.; Wang, X.; Fang, Q.; Liu, X.; Li, Y.; Xue, F. Internal friction study on precipitation/dissolution of Mn-Ni-Si phase in aged RPV model steel. *Mater. Lett.* **2020**, *269*, 127668. [CrossRef]
19. Liu, X.; Sun, M.; Hao, T.; Jiang, W.; Wang, X.; Fang, Q. Interplay between carbon and substitutional solute atoms during precipitation of Mn/Ni/Si-rich phases in model reactor pressure vessel steels. *Scr. Mater.* **2023**, *225*, 115158. [CrossRef]
20. Liu, X.; Sun, M.; Ke, Y.; Wang, X.; Hao, T.; Jiang, W.; Wang, X.; Fang, Q. Solute atom migration and evolution of C-bearing Mn-Ni-Si-rich precipitates in RPV steel during the early aging period. *J. Mater. Sci. Technol.* **2026**, *246*, 44–57. [CrossRef]
21. Jiao, Z.B.; Luan, J.H.; Miller, M.K.; Yu, C.Y.; Liu, C.T. Group precipitation and age hardening of nanostructured Fe-based alloys with ultra-high strengths. *Sci. Rep.* **2016**, *6*, 21364. [CrossRef] [PubMed]
22. Yang, M.; Zhu, J.; Yang, T.; Luan, J.; Jiao, Z.; Fan, X.; Kuhn, B.; Xiong, X.; Wang, C.; Liu, C.T.; et al. A novel ferritic steel family hardened by intermetallic compound G-phase. *Mater. Sci. Eng. A* **2019**, *745*, 390–399. [CrossRef]
23. Li, C.; Shu, G.; Liu, W.; Duan, Y. Effects of neutron irradiation on elastic modulus of RPV steel. *Ann. Nucl. Energy* **2019**, *134*, 20–26. [CrossRef]
24. Miyajima, Y.; Komatsu, S.Y.; Mitsuhara, M.; Hata, S.; Nakashima, H.; Tsuji, N. Change in electrical resistivity of commercial purity aluminium severely plastic deformed. *Philos. Mag.* **2010**, *90*, 4475–4488. [CrossRef]
25. Miyajima, Y.; Komatsu, S.Y.; Mitsuhara, M.; Hata, S.; Nakashima, H.; Tsuji, N. Microstructural change due to isochronal annealing in severely plastic-deformed commercial purity aluminium. *Philos. Mag.* **2015**, *95*, 1139–1149. [CrossRef]
26. Deng, L.; Seagle, C.; Fei, Y.; Shahar, A. High pressure and temperature electrical resistivity of iron and implications for planetary cores. *Geophys. Res. Lett.* **2013**, *40*, 33–37. [CrossRef]
27. Li, C.; Shu, G.; Liu, Y.; Huang, Y.; Chen, J.; Duan, Y.; Liu, W. Effects of neutron irradiation on resistivity of reactor pressure vessel steel. *J. Nucl. Mater.* **2018**, *499*, 446–450. [CrossRef]
28. Chen, C.W. Saturation moments and residual resistivities of iron-cobalt ternary alloys. *Philos. Mag.* **1962**, *7*, 1753–1764. [CrossRef]
29. Domenicali, C.A.; Otter, F.A. Thermoelectric Power and Electrical Resistivity of Dilute Alloys of Silicon in Copper, Nickel, and Iron. *J. Appl. Phys.* **1955**, *26*, 377–380. [CrossRef]
30. Bohnenkamp, U.; Sandström, R.; Grimvall, G. Electrical resistivity of steels and face-centered-cubic iron. *J. Appl. Phys.* **2002**, *92*, 4402–4407. [CrossRef]
31. Xue, J.; Hu, R.; Bai, G.; Mei, J.; Xue, F.; Sha, G. Temperature-Dependent Irradiation-Induced Clustering in a Fe-Mn-Ni Alloy. *Metall. Mater. Trans. A* **2021**, *52*, 4264–4274. [CrossRef]
32. Odette, G.R.; Wirth, B.D. A computational microscopy study of nanostructural evolution in irradiated pressure vessel steels. *J. Nucl. Mater.* **1997**, *251*, 157–171. [CrossRef]
33. Garrett, A. Simulation of Precipitate Formation Under Neutron Irradiation in Low-Alloy Pressure Vessel Steels. Ph.D. Thesis, The University of Manchester, Manchester, UK, 2021.
34. Mamivand, M.; Wells, P.; Ke, H.; Shu, S.; Odette, G.R.; Morgan, D. CuMnNiSi precipitate evolution in irradiated reactor pressure vessel steels: Integrated Cluster Dynamics and experiments. *Acta Mater.* **2019**, *180*, 199–217. [CrossRef]
35. Zelenty, J.E. Understanding thermally induced embrittlement in low copper RPV steels utilising atom probe tomography. *Mater. Sci. Technol.* **2015**, *31*, 981–988. [CrossRef]
36. Fujii, K.; Fukuya, K.; Nakata, N.; Hono, K.; Nagai, Y.; Hasegawa, M. Hardening and microstructural evolution in A533B steels under high-dose electron irradiation. *J. Nucl. Mater.* **2005**, *340*, 247–258. [CrossRef]
37. Liu, X.; Sun, M.; Ke, Y.; Wang, X.; Hao, T.; Jiang, W.; Wang, X.; Fang, Q. Re-dissolution of precipitates in reactor pressure vessel steels evaluated by internal friction technique. *Mater. Lett.* **2024**, *359*, 135916. [CrossRef]
38. Fedotova, S.V.; Kuleshova, E.A.; Gurovich, B.A.; Frolov, A.S.; Maltsev, D.A.; Zhuchkov, G.M.; Fedotov, I.V. APT studies of phase formation features in VVER-440 RPV weld and base metal in irradiation-annealing cycles. *J. Nucl. Mater.* **2018**, *511*, 30–42. [CrossRef]

Disclaimer/Publisher's Note: The statements, opinions and data contained in all publications are solely those of the individual author(s) and contributor(s) and not of MDPI and/or the editor(s). MDPI and/or the editor(s) disclaim responsibility for any injury to people or property resulting from any ideas, methods, instructions or products referred to in the content.